Nuclear Science and Techniques (2024) 35:47
https://doi.org/10.1007/s41365-024-01396-3

# Normalized glandular dose coefficients for digital breast tomosynthesis using detailed Chinese breast models

Jia-Hao Wang[1,2] · Rui Qiu[1,2] · An-Kang Hu[1,2] · Ye-Qi Liu[1,2] · Zhen Wu[3] · Hui Zhang[1,2] · Jun-Li Li[1,2]

Received: 1 June 2023 / Revised: 16 August 2023 / Accepted: 13 September 2023 / Published online: 9 April 2024


## Abstract

The rise in breast cancer diagnoses among Chinese women has necessitated the use of X-ray breast screening, which carries a radiation risk. This study aimed to provide a dosimetry protocol for the Chinese female population to replace the traditional standard that utilizes simplified breast models, for the accurate estimation of the mean glandular dose of a patient undergoing digital breast tomosynthesis (DBT). The first set of detailed Chinese female breast models and representative breast parameters was constructed. Considering backscatter radiation and computational efficiency, we improved the combination of these models and the Chinese reference adult female whole-body voxel phantom. Image acquisition for four commercial DBT systems that are widely employed in China was simulated using the Monte Carlo method to obtain the normalized glandular dose coefficients of DBT $\left(D_{\mathrm{gN}}^{\mathrm{DBT}}\right)$ and the glandular depth dose $\left(D_{\mathrm{g}}^{\mathrm{dep}}(z)\right)$ for different breast characteristics and X-ray spectra. We calculated a series of $D_{\mathrm{gN}}^{\mathrm{DBT}}$ values for breasts with different percentage mass glandularities (5%, 25%, 50%, 75%, and 100%) and compressed breast thicknesses (2, 3, 4, 5, 6, and 7 cm) at various tube potentials (25, 28, 30, 32, 35, and 49 kV) and target/filter combinations (W/Rh, W/Al, Mo/Mo, Rh/Rh, and Rh/Ag). The parameter dependence of the breast characteristics and beam conditions on $D_{\mathrm{gN}}^{\mathrm{DBT}}$ in detailed breast models was investigated. The $D_{\mathrm{gN}}^{\mathrm{DBT}}$ results were 14.6–51.0% lower than those of the traditional dosimetry standard in China. The difference in $D_{\mathrm{gN}}^{\mathrm{DBT}}$ was mainly due to a decrease in the depth of the main energy deposition area caused by the glandular distribution along the depth direction. The results obtained in this study may be used to improve breast dosimetry in China and provide more detailed information on risk assessment during DBT.

**Keywords** Digital breast tomosynthesis · Normalized glandular dose coefficients · Detailed breast model · Monte Carlo simulation

## 1 Introduction

Breast cancer is the most common cancer among women in China, with more than 400,000 cases annually [1–3]. Digital mammography is the primary screening method for breast cancer. An improved version of mammography, known as digital breast tomosynthesis (DBT), that offers "pseudo-3D" information and more accurate screening results is gaining popularity in China [4, 5]. However, the radiation effects of DBT on patients require further investigation. Meanwhile, ICRP-Report 103 has revised the tissue weight factor of breasts from 0.05 to 0.12 [6]. Therefore, radiation-induced breast cancer risk in the Chinese female population should be carefully considered for breast X-ray imaging, especially DBT.

This work was supported by the National Natural Science Foundation of China (Nos. U2167209 and 12175114) and the National Key R&D Program of China (No. 2021YFF0603600).

✉ Rui Qiu
qiurui@tsinghua.edu.cn

[1] Department of Engineering Physics, Tsinghua University, Beijing 100084, China

[2] Key Laboratory of Particle and Radiation Imaging, Ministry of Education, Tsinghua University, Beijing 100084, China

[3] Joint Institute of Tsinghua University, Nuctech Company Limited Beijing, Beijing 100084, China

A widely accepted quantity for breast dosimetry protocols is the mean glandular dose $(D_g)$, which reflects the high radiosensitivity of glandular tissues [7]. The breast dosimetry protocol used in China follows the simple breast model proposed by Dance et al. [8, 9]. This model consists of a central region with a uniform mixture of glandular and adipose tissues and a peripheral 5-mm-thick "subcutaneous adipose region." However, this simple model does not represent the actual anatomical structure of the breast. It is widely agreed that the use of simplified homogeneous models instead of heterogeneous breast models can lead to the overestimation of $D_g$ [10–13]. In recent years, researchers have attempted to obtain breast parameters that influence $D_g$, including skin thickness [11, 14, 15], subcutaneous adipose layer thickness [15] and glandular distribution [10, 12, 16–18], using high-resolution clinically dedicated breast computed tomography (DBCT) images. The literature verifies that to achieve an accurate estimation of $D_g$, more accurate characteristics of the breast must be considered in breast dosimetry protocols.

The anatomical parameters of the breast vary significantly among different races [19–22]. These differences in anatomical characteristics may result in inaccurate estimations of $D_g$ from the patient. Previous studies have shown that using a human phantom based on Caucasian rather than Chinese characteristics can result in more than a 50% difference in $D_g$ with the same irradiation pattern [23, 24]. The breast volumes of Caucasians, African Americans, and Hispanics are larger than that of Asians, and the breasts of Caucasian women are denser than those of Asian women.

Even though several heterogeneous breast models have been constructed for the development of breast dosimetry, they are mainly based on the breast characteristics of Western women [8, 9]. According to the breast metrics examined through DBCT data in the USA [25], Hernandez constructed a breast model enclosed by a 1.5 mm skin layer as a half-elliptical shape using three elliptic radii. Glandular fraction values were assigned to each contoured region using a fitted Gauss distribution [17]. A new voxel model that considers a heterogeneous glandular distribution was created by Tucciariello [26]. To characterize the amount and distribution of glandular tissue in patient breasts during compression, 88 DBCT datasets were acquired from a medical center in the Netherlands for clinical trials [18]. The distributions along the three directions were used to define the internal tissue distributions for the cranio-caudal (CC) and medio-lateral-oblique (MLO) models. However, there is no literature on dosimetry research on the breast characteristics of Chinese women. Therefore, to ensure accurate dose estimation, it is crucial to establish breast dosimetry suitable for Chinese women.

In a previous study, we conducted a retrospective review based on the clinical mammography data of Chinese women, in which we statistically analyzed their anatomical parameters. These parameters differ in breast volume, typical glandular fraction, and subcutaneous adipose thickness compared to those in Western women. Based on these representative breast parameters, we developed the first set of detailed breast models for Chinese females and used these models to calculate $D_{gN}$, which has been adopted by the Chinese specification for testing quality control in X-ray mammography [27–32].

In this study, we aimed to calculate the normalized glandular dose coefficients $\left(D_{gN}^{DBT}\right)$ for four commercial DBT devices, which are the main foreign DBT manufacturers in China, and analyze the parameter dependence of breast characteristics and beam conditions on $D_{gN}^{DBT}$ when considering the detailed structure inside the breast. We compared $D_{gN}^{DBT}$ in the traditional and improved breast dosimetry protocols for the Chinese female population and analyzed the reasons for the differences based on the dose distribution along the depth direction of simple and detailed breast models.

## 2 Materials and methods

### 2.1 Improved dosimetry protocol for DBT

$D_{gN}^{DBT}$, which is the most essential quantity for estimating the $D_g$ of patients, was calculated for each combination of equipment geometry, X-ray spectrum, and breast model using Monte Carlo (MC) simulations. These values, expressed in mGy/mGy, represent the ratio of $D_g^{DBT}$ (in mGy) to the incident air kerma $(K_{air})$ (in mGy) at the reference point without considering backscatter. The reference point was positioned along the central axis of the upper surface of the breast, 4 cm from the edge of the detector closest to the chest wall. For each spectrum and target/filter combination, the half-value layer (HVL) was calculated using MC simulations [33] and expressed as the aluminum thickness with equivalent attenuation properties.

$D_g$ is significantly affected by the depth of the major energy deposited in the glandular tissue. MC simulations have demonstrated that the dose distribution during mammography exhibits a high degree of heterogeneity [13, 34]. The deposited dose in nearly 40% of glandular voxels was found to exceed the $D_g$ within the breast model with a 4-cm compressed breast thickness (CBT) and 50% glandularity [34]. An alternative dose metric known as glandular depth dose $\left(D_g^{dep}(z)\right)$ has been suggested to investigate the differences in $D_g^{DBT}$ between breast models with different glandular distributions [13, 34]. $D_g^{dep}(z)$ provides more detailed information on the distribution of the radiation dose along the depth direction, especially in areas with dense glandular

tissue. Specifically, $D_g^{dep}(z)$ is defined as the glandular dose deposited in a specific slice at depth $z$.

To better understand the contribution of each voxel slice of the detailed breast model to $D_g$, we used a physical quantity: the normalized deposited energy in the glandular tissue at slice depth $z$, $E_{gN}(z)$, which can be calculated using the following equation:

$$E_{gN}(z) = \frac{D_g^{dep}(z)}{D_g} \cdot \frac{m_g(z)}{m_g} = \frac{D_g^{dep}(z)}{D_g} \cdot f_g(z), \quad (1)$$

where $m_g(z)$ is the glandular mass at slice depth $z$, and $f_g(z)$ is a function that represents the distribution of the glandular mass along the depth direction.

In traditional dosimetry, the $D_{gN}$ coefficients measure the $D_g$ undergoing mammography equivalently as multiplication results of the factors $g$, $c$, and $s$ in Dance's equation [8, 9, 35]. The $g$-factor is a dose conversion factor calculated under different spectra with reference to the breast model with 50% glandularity at different CBTs. The $c$- and $s$-factors are adjusted for an X-ray spectrum different from that of the Mo/Mo target/filter and glandularity different from 50%, respectively. The relative differences $\Delta$ of $D_{gN}^{DBT}$ between the improved and traditional breast dosimetry can be calculated via

$$\Delta = \frac{gcsT - D_g^{DBT}}{gcsT} \times 100\%, \quad (2)$$

where $g$, $c$, $s$, $T$, and $D_{gN}^{DBT}$ are the conversion factors under the same breast characteristics and beam conditions, corresponding to the traditional dosimetry standard and this study.

## 2.2 Detailed breast model and the improved combination with CRAF

In a previous study, we identified typical parameters of the breast, including external parameters such as the base diameter of the breast, the distance from the nipple to chest wall, skin thickness, and subcutaneous adipose thickness [28, 36]. Based on the assumptions of Bakic et al. [37] and Mahr et al. [38] regarding the anatomical growth of the lactiferous ducts and glandular tissue in the fibroglandular region, we altered the glandular distribution by randomly sampling adipose lobules to replace the glandular tissue. This allowed us to approximate the glandular distribution of our target breast model as close to that observed in clinical settings. The percentage of glandular tissue and the CBT in our target models were typical parameters selected from those reported for Chinese women in clinical statistics [28].

Based on the representative breast parameters, we developed the first set of detailed breast models for Chinese females. Table 1 lists the voxel sizes of models with different glandularities and CBTs. Each voxel represented a unique tissue. As the CBT decreased, the voxel size in the depth direction decreased to ensure the completeness of detail in the breast models. These models included four breast regions: skin, the adipose tissue region (subcutaneous adipose, posterior adipose, and Cooper's ligaments), fibroglandular region (intraglandular adipose, glandular, lactiferous ducts, and lobules), and nipple region (lactiferous sinus and adipose). The skin thickness was set at 1.45 mm. The thickness of the subcutaneous adipose layer was set at 4 mm near the nipple and slightly greater than 4 mm near the chest wall. The fibroglandular region was the central region in the breast model, excluding the skin, subcutaneous adipose layer, and posterior adipose layer, similar to the central region in the simple breast model of the traditional standard. Detailed breast models with glandularity levels of 5%, 25%, 50%, 75%, and 100% were constructed. Glandularity is a physical quantity that indicates the proportion of glandular tissue and can be expressed as percentage volume or percentage mass glandularity. The percentage mass glandularity $\left(P_g^M\right)$ can be calculated using

$$P_g^M = \frac{m_g}{M_{fg}} \times 100\%, \quad (3)$$

**Table 1** Voxel size of detailed breast models with different glandularities and CBTs

| CBT (cm) | Voxel size (mm × mm × mm) | | | | |
|---|---|---|---|---|---|
| | $P_g^M$(%) | | | | |
| | 5 | 25 | 50 | 75 | 100 |
| 2 | 0.2×0.2×0.050 | 0.2×0.2×0.050 | 0.2×0.2×0.050 | 0.2×0.2×0.050 | 0.2×0.2×0.050 |
| 3 | 0.2×0.2×0.070 | 0.2×0.2×0.068 | 0.2×0.2×0.064 | 0.2×0.2×0.058 | 0.2×0.2×0.054 |
| 4 | 0.2×0.2×0.087 | 0.2×0.2×0.085 | 0.2×0.2×0.081 | 0.2×0.2×0.076 | 0.2×0.2×0.072 |
| 5 | 0.2×0.2×0.103 | 0.2×0.2×0.101 | 0.2×0.2×0.098 | 0.2×0.2×0.094 | 0.2×0.2×0.090 |
| 6 | 0.2×0.2×0.119 | 0.2×0.2×0.117 | 0.2×0.2×0.115 | 0.2×0.2×0.111 | 0.2×0.2×0.108 |
| 7 | 0.2×0.2×0.129 | 0.2×0.2×0.128 | 0.2×0.2×0.126 | 0.2×0.2×0.121 | 0.2×0.2×0.119 |

where $m_g$ is the mass of the glandular tissue, and $M_{fg}$ is the total mass of the fibroglandular region. The percentage volume glandularity $\left(P_g^V\right)$ can be calculated via

$$P_g^V = \frac{V_g}{V_{br}} \times 100\%, \tag{4}$$

where $V_g$ is the volume of the glandular tissue, and $V_{br}$ is the volume of the breast model. The corresponding $P_g^V$ values for models with 5%, 25%, 50%, 75%, and 100% $P_g^M$ were 1.6%, 8.2%, 16.6%, 25.4%, and 34.4%. In the fibroglandular region, the 5% $P_g^M$ model contained only lactiferous ducts and intraglandular adipose tissue, whereas the 100% $P_g^M$ model contained only glandular tissue. Models with different glandularities were constructed by altering the number of adipose globules whose central points were uniformly sampled within the fibroglandular region.

Vertical slices of each breast model with different glandularities were deformed to compress these models to 2, 3, 4, 5, 6, and 7 cm in the CC view. This resulted in 30 compressed breast models for dose estimation in DBT. The compression algorithm divides the breast model into skin, the adipose tissue region, and fibroglandular tissue region and calculates the elasticity parameters of the breast tissues based on ultrasound velocity measurements and tissue densities. The algorithm separately compresses each vertical slice of breast tissue using the elastic modulus of the corresponding tissue region and determines the amount of compression based on the strain, which is calculated using the change in the thickness of the breast tissue. The algorithm preserves the volume of the breast during compression, as biological materials are considered incompressible, and considers the original dimensions and thicknesses of the breast model to calculate the final compressed dimensions [28]. Detailed breast models, in which the glandular tissue tends to be more concentrated in the central part of the sagittal plane, have glandular distributions that are different from those of the simple model. Previous research has indicated that, based on the simple breast model, the beam condition (target/filter combination, beam HVL) and breast characteristics (CBT and glandularity) are the main influencing factors of $D_{gN}^{DBT}$, in addition to the tomosynthesis system specifications [39].

To investigate the difference in $D_{gN}^{DBT}$ between the detailed and simple breast models, we constructed a series of homogeneous breast models with 4 cm CBT and 25%, 50%, 75%, and 100% $P_g^M$ by uniformly sampling the glandular voxels in the central part.

In our previous study, we combined the compressed breast model with the Chinese reference adult female whole-body voxel phantom (CRAF) to account for backscatter radiation from the female body. However, this reduced the computational efficiency of the MC simulation owing to the

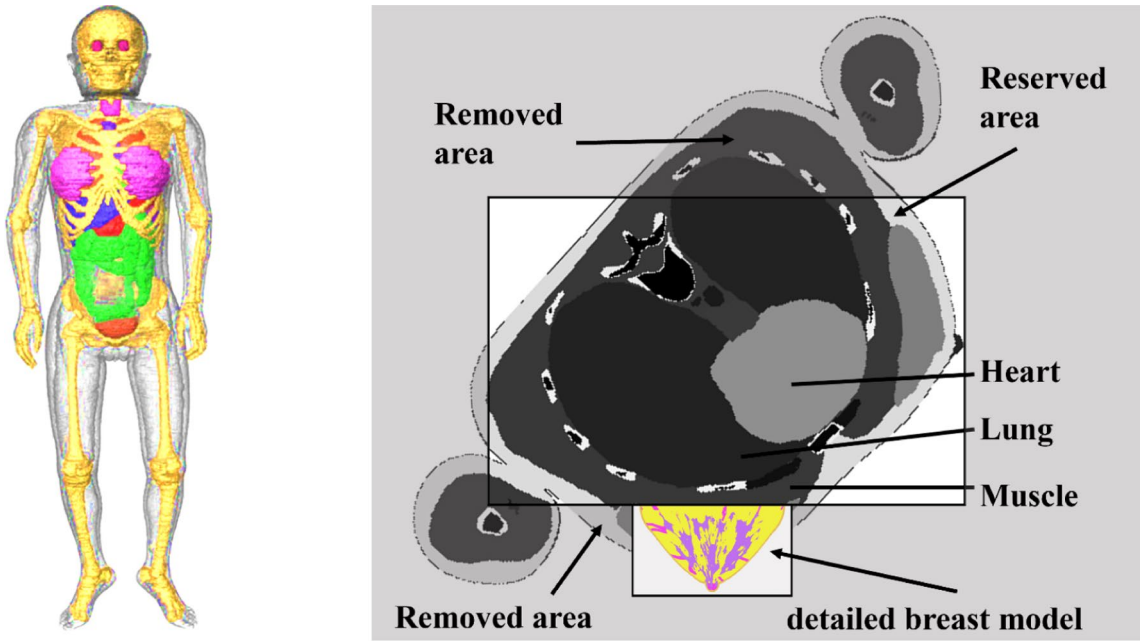


**Fig. 1** **a** 3D display of the CRAF model, where the pink region represents the breast organ in CRAF. **b** Improved method to combine the breast model and CRAF. The major organs, including the heart, lung, and posterior muscle of the breast, were reserved, and the body tissue away from the breast was removed. The breast organ in CRAF was replaced via the detailed breast model. (Color figure online)

millions of voxels in CRAF. To enhance the efficiency and accuracy of the MC simulation, we improved the geometric construction of CRAF. According to the position of the breast in the female body, CRAF was rotated and cropped, and the major organs and tissues that provided backscattered particles were present. During construction of the imaging geometry, the nipple of the breast model was aligned with that of CRAF. The CRAF and cropped CRAF models are shown in Fig. 1.

### 2.3 Irradiation geometries

The simulation geometry used to calculate two quantities, $D_g$ and $D_g^{dep}(z)$, is shown in Fig. 2a. The geometry consisted of an X-ray tube and a series of geometric components. The X-ray tube had an X-ray source and a filter below it, which was employed for energy spectrum hardening. During the scanning process, the source and filter rotated together along the orbit around the center of rotation. The geometric components included a compression paddle, breast model, support paddle, and image receptor, which were aligned with the chest wall plane. The compression paddle was constructed from polycarbonate, whereas the support paddle was composed of carbon fiber. An air gap existed between the support paddle and the image receptor. The position of the compression paddle placed on top of the breast model changed with the CBT. The isotropic particle emission was set up at a cone angle that covered the image receptor edge. Four commercial scanning geometries were constructed. The device parameters are listed in Table 2.

To simulate $K_{air}$, the breast model and support paddle were eliminated and a cylindrical air-filled ionization chamber (15 mm radius, 10 mm height) was positioned at the breast entrance plane [8, 40]. The compression paddle was elevated 40 cm above the upper plane of the ionization chamber to reduce scattered radiation from the paddle [8]. Air filled the world in all the simulations. The simulation geometry is illustrated in Fig. 2b.

### 2.4 Monte Carlo simulation

A previous MC computer program for mammography dosimetry was modified to calculate $D_g$ for DBT using the Geant4 (version 10.6) simulation toolkit [41]. The irradiation geometries are described in detail in Sect. 2.3. A detailed validation of the mammography dosimetric program can be found in [28]. A simple breast model with 4 cm CBT and 50% $P_g^M$ was constructed using voxels to validate the

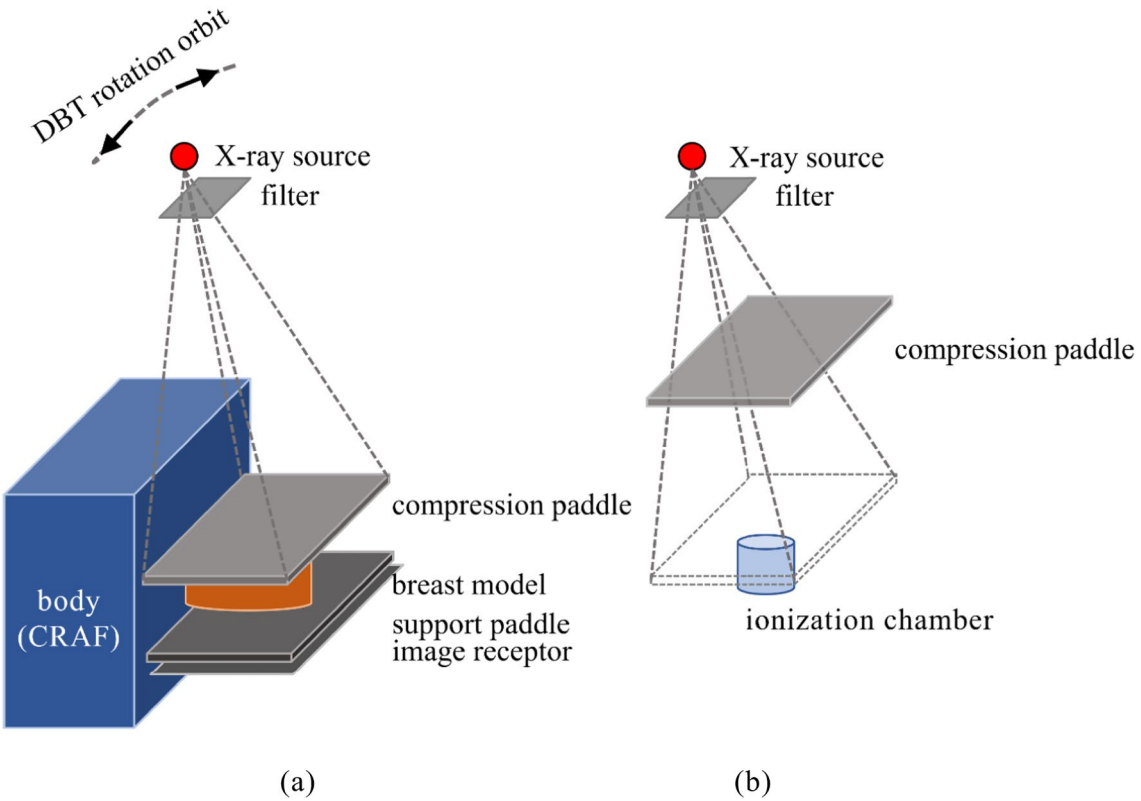


**Fig. 2** Irradiation geometry to measure **a** glandular dose and **b** $K_{air}$. (Color figure online)

**Table 2** Imaging parameters of manufacturers' devices

| | DBT systems | | | |
|---|---|---|---|---|
| | Siemens mammomat inspiration | Hologic selenia dimensions | GE SenoClaire | GE senographe pristina |
| Scan angle, $\Delta\alpha(^\circ)$ | 50(i.e. ±25) | 15(i.e. ±7.5) | 25(i.e. ±12.5) | 25(i.e. ±12.5) |
| Number of projections, $N$ | 25 | 15 | 9 | 9 |
| Anode target/filter combination | W/Rh 50 μm | W/Al 700 μm | Mo/Mo 30 μm<br>Rh/Rh 25 μm | Mo/Mo 30 μm<br>Rh/Ag 50 μm |
| Distance source to the detector (DSD) (mm) | 655 | 700 | 660 | 660 |
| Distance detector to rotation (DDR) (mm) | 608 | 700 | 620 | 617 |
| Distance of air gap (DAG) (mm) | 17 | 25 | 22 | 23 |
| Detector field (mm × mm) | 240 × 300 | 240 × 290 | 239 × 306 | 240 × 286 |
| Compression paddle material | Polycarbonate | Polycarbonate | Polycarbonate | Polycarbonate |
| Compression paddle thickness (mm) | 2.8 | 2.8 | 2.7 | 2.7 |
| Carbon fiber support paddle thickness (mm) | 2.0 | 1.0 | 1.4 | 1.4 |
| Ref | [33] | [33] | [33] | [33] |

modification of the X-ray tube rotation angle. This model had a uniform distribution of voxels labeled as glandular and adipose in the central part. Four different spectra (Mo/Mo 25 kV, Rh/Rh 29 kV, W/Rh 34 kV, and W/Ag 40 kV) were used to irradiate the model for projections from 0° to 30° in 5° increments.

Dosimetry quantities, glandular doses, and $K_{air}$ were estimated using independent MC simulations. Only photons were considered in the simulations (cutoff energy of 10 eV and cutoff length of 0.1 mm). All the secondary electrons were regarded as being locally deposited. The number of photons simulated for $D_g$ was between $10^8$ and $10^9$, depending on the parameters of the input models (breast glandularity and CBT). The statistical uncertainties for glandular dose and $K_{air}$ were less than 1%. The simulations were conducted using an Intel® Xeon® CPU E5-2680@2.3 GHz. The computational time required to process $10^8$ photons using a single core was several hours. The calculation speed was significantly improved to ensure simulation accuracy. To ensure that the statistical uncertainty for $D_g^{dep}(z)$ at all depths was less than 1%, the number of photons simulated for $D_g^{dep}(z)$ was set to $1.3 \times 10^{10}$. Python (v. 3.9) [42] scripts were written to generate input files and shell scripts for simulation automation.

The properties of adipose, glandular, and skin tissues, including their composition and density, were obtained from ICRU-Report 46 [43]. Values for Cooper's ligament tissue in the detailed breast model were not specifically provided by the ICRU; therefore, the density and element composition of Cooper's ligament tissue were substituted with those of muscular fibrous tissue [38].

The polychromatic X-ray spectra acquired from the spectral models of Boone et al. [44] and Hernandez et al. [45] were simulated. Simulations were conducted to cover the typical parameters available in clinical systems using various tube potentials (25, 28, 30, 32, 35, and 49 kV) and target/filter combinations (W/Rh, W/Al, Mo/Mo, Rh/Rh, and Rh/Ag). The polychromatic spectra exhibited an energy resolution of 0.5 keV. The heeling effect was not implemented.

## 3 Results

### 3.1 Validation for simulation methods

As shown in Fig. 3, the $t$-factors reported by Dance et al. [9], which capture the variation in $D_{gN}$ due to nonzero projection angles of an X-ray source, were compared with those generated using the MC code employed in this study for four spectra and projection angles $\alpha$ ranging from 0° to 30°. These

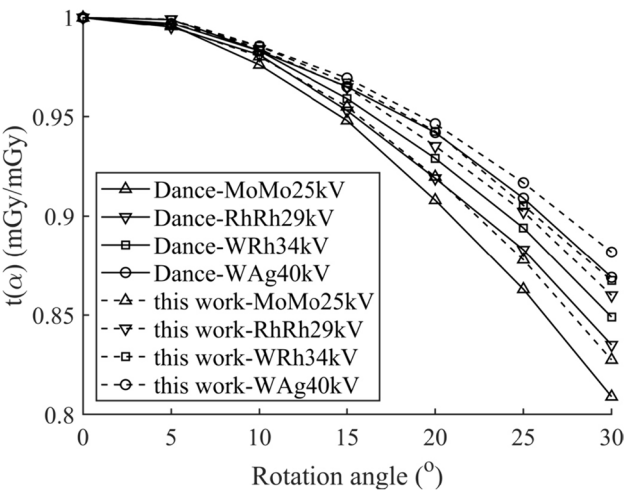


**Fig. 3** Comparison between the validated results and Dance's data

**Table 3** Computation time and difference in the results (compared to the improved combination) of the three model combinations

| Combination | Particles | Computation time (h) | Difference (%) |
|---|---|---|---|
| Breast | $1 \times 10^8$ | ~2 | −2.4% |
| CRAF + breast | $5 \times 10^6$ | ~10 | 0.7% |
| CRAF + breast (improved) | $1 \times 10^8$ | ~5 | 0 |

results are consistent with data obtained by Dance et al. All data differed within 3%, with the largest difference occurring when the angle was largest. The main reason for this variation is the method used to construct the simple model. The energy deposited in the adipose and glandular tissues in the central region of the simple breast model adopted by Dance was calculated based on the probability of interaction between the two tissues. However, the energy deposited in the glandular tissue could be obtained directly because of the separation of the adipose and glandular tissues in the voxel model used in this study.

## 3.2 Improved computational efficiency and accuracy considering backscatter

Table 3 lists the MC simulation computation times and the differences between the three combinations under the same irradiation parameters and breast model. These combinations included breasts without CRAF, CRAF + breast, and CRAF + breast (improved). The results obtained without considering backscattering were 2.4% lower than those obtained when considering body backscattering. This was because posterior adipose tissue existed in the model itself, which provided a portion of the backscatter dose for the glandular tissue. However, the presence of CRAF still resulted in more accurate simulation results. Compared with the combination method of the female body, which wasted considerable computational time in unnecessary organ voxels for particle transport [28], the improved method adopted in this study only retained the main body and organs that produced backscatter particles for glandular tissue. This resulted in a significant improvement (approximately 40 times) in computation speed while ensuring computational accuracy. This allowed us to simulate a large number of particles in a short period (several hours) and reduce statistical errors in the dose.

## 3.3 Normalized glandular dose—$D_{gN}^{DBT}$

### 3.3.1 Parameter dependence of breast characteristics and beam conditions on $D_{gN}^{DBT}$

The dependence of various model parameters on $D_{gN}^{DBT}$ must be investigated based on a detailed breast model. In the simulation, four breast models with different CBTs (4 cm and 5 cm) and $P_g^M$ (25% and 50%) were used for irradiation. We calculated the HVL for the energy spectra at different tube voltages and two target/filter combinations of Mo/Mo and W/Rh and found a good linear relationship between the HVL and $D_{gN}^{DBT}$. Linear regression analysis showed high consistency ($R^2 > 0.999$) and low residual error (within $1 \times 10^{-3}$) for Mo/Mo (Fig. 4a), and a good consistency

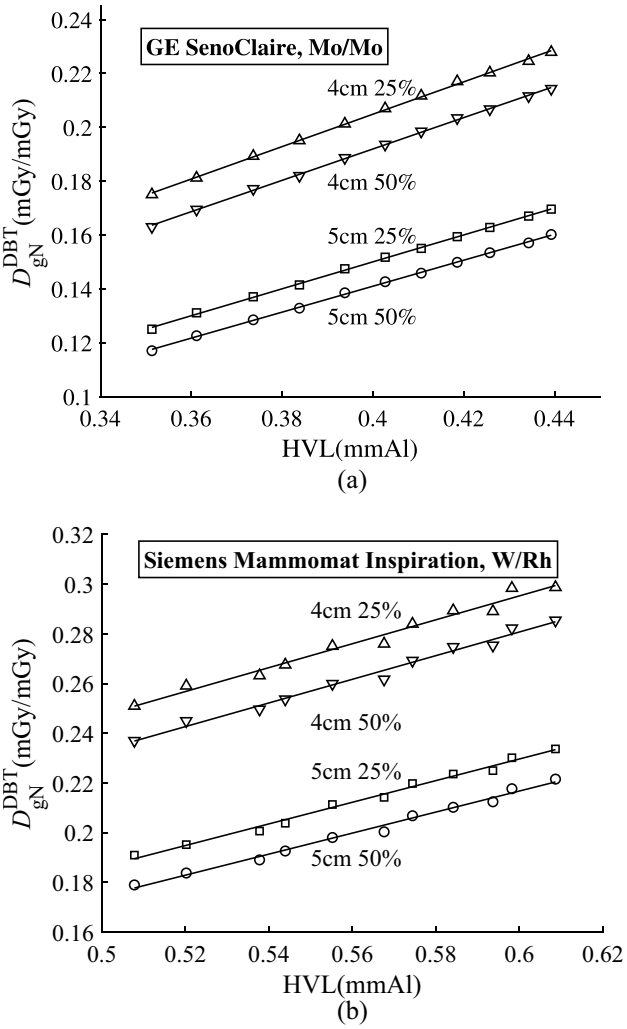


**Fig. 4** $D_{gN}^{DBT}$ values calculated for the **a** Mo/Mo and **b** W/Rh Target/Filter combination, and their linear fit (continuous lines) with varying beam HVL

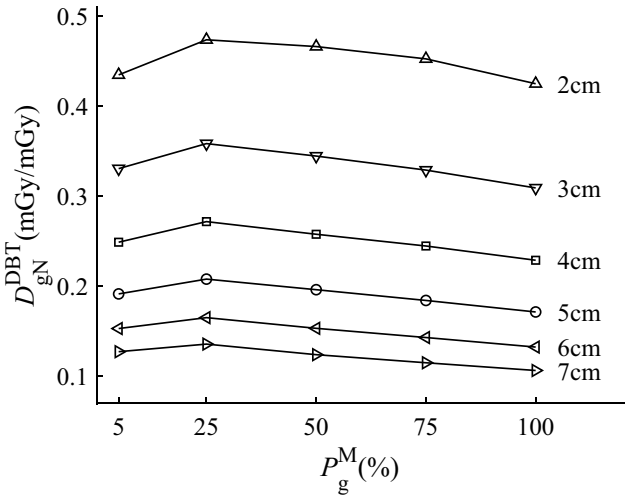


**Fig. 5** Varying $D_{gN}^{DBT}$ values with $P_g^M$ for different CBTs and the target/filter combination of W/Rh at 28 kVp

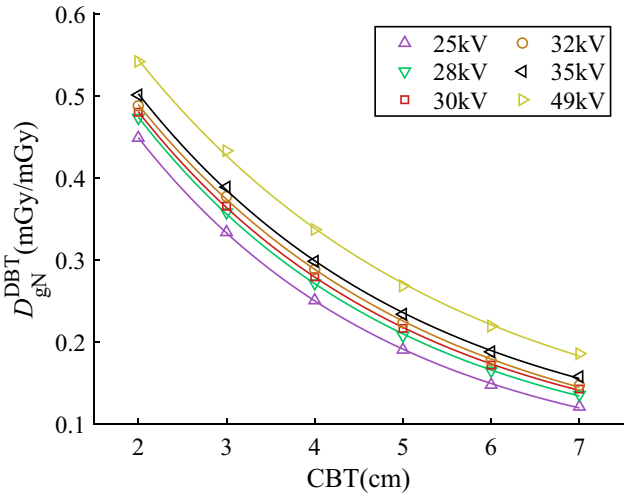


**Fig. 6** $D_{gN}^{DBT}$ values calculated for the W/Rh target/filter combination and bi-exponential fit (continuous lines) with varying CBTs. (Color figure online)

($R^2 > 0.95$) and a moderate residual error (within $4 \times 10^{-3}$) for W/Rh (Fig. 4b).

Figure 5 shows the relationship between $D_{gN}^{DBT}$ and the glandularity for different CBTs and the target/filter combination of W/Rh at 28 kVp. $D_{gN}^{DBT}$ values generally decreased as the $P_g^M$ concentration increased from 25 to 100%. However, we also observed an unexpected result: the model with 5% glandularity had a lower $D_{gN}^{DBT}$ than that with 25% $P_g^M$. This result contradicts the results obtained from literature based on simple breast models [9, 39]. The possible reasons for this discrepancy are discussed in the following section.

We examined the relationship between $D_{gN}^{DBT}$ and CBT at different tube voltages by setting the $P_g^M$ of the breast models to 25%. These data were fitted to the bi-exponential function proposed by Sobol and Wu (1997), which describes the relationship between $D_{gN}^{DBT}$ and CBT. The regression analysis revealed that this function accurately modeled our data (Fig. 6) with a high goodness of fit ($R^2 > 0.99$) and low residual error (within $4 \times 10^{-3}$).

### 3.3.2 $D_{gN}^{DBT}$ tabulation for commercial devices

For the DBT devices widely used in China, Tables 4, 5, 6, 7 and 8 in Appendix A list the $D_{gN}^{DBT}$ values for different target/filter combinations: HVL, CBT, and $P_g^M$. As illustrated in Table 1, the imaging geometry parameters of GE SenoClaire and GE Senographe Pristina were almost equal. The difference in $D_{gN}^{DBT}$ for the Mo/Mo target filtration between these two devices was within 0.5%. The data in Table 6 can be used for the dose estimation of the Mo/Mo target filtration for both devices. The results from the other devices were significantly influenced by the target/filter combination when the HVL, CBT, and $P_g^M$ parameters were fixed. These coefficients can also be applied to estimate the $D_g$ for breasts with the corresponding $P_g^V$.

## 3.4 Glandular depth dose—$D_g^{dep}(z)$

We performed simulations on detailed and simple breast models with different $P_g^M$: 25%, 50%, 75%, and 100%. Each model had the same CBT value of 4 cm. The glandular tissue in the detailed models was not uniformly distributed along the depth direction, as shown in Fig. 7a. We used a W/Rh 28 kV beam to irradiate these breast models and calculated the normalized $D_g^{dep}(z)$ for each model. Figure 7b compares the normalized $D_g^{dep}(z)$ curves for the detailed models and shows the relative errors of these four models during the MC simulation in the top-right corner. The linear attenuation coefficients of the models depended on the glandularity. As glandularity increased, so did the linear attenuation coefficient, because the density and equivalent attenuation coefficient of glandular tissue are larger than those of adipose tissue. Figure 7c shows a comparison of $E_{gN}(z)$ between the detailed and simple models. For the simple model, most of the deposited energy in the glandular tissue was concentrated in the upper surface of the central region, but for detailed models, the main

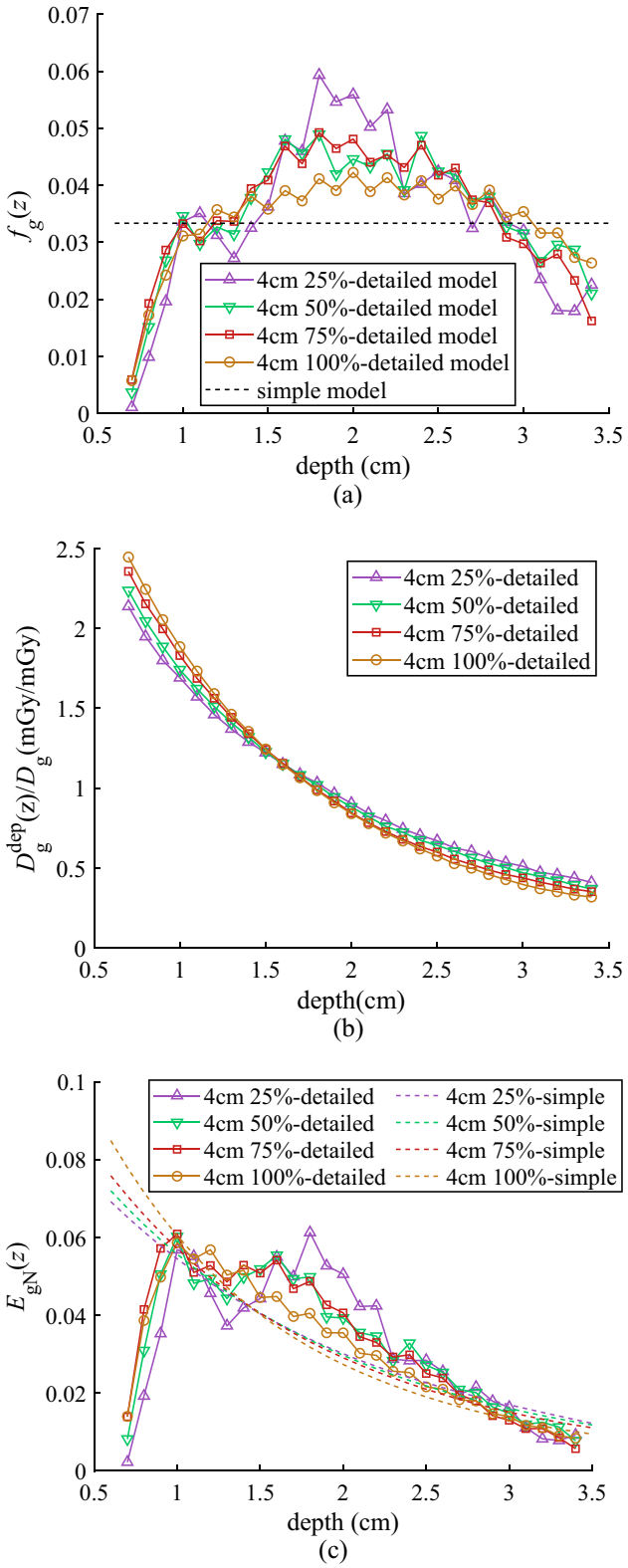


**Fig. 7** **a** Glandular fraction along the $z$ direction of detailed and simple breast models. **b** Normalized $D_g^{dep}(z)$ curves of detailed breast models with different $P_g^M$: 25%, 50%, 75%, and 100%. **c** $E_{gN}(z)$ of detailed and simple models. (Color figure online)

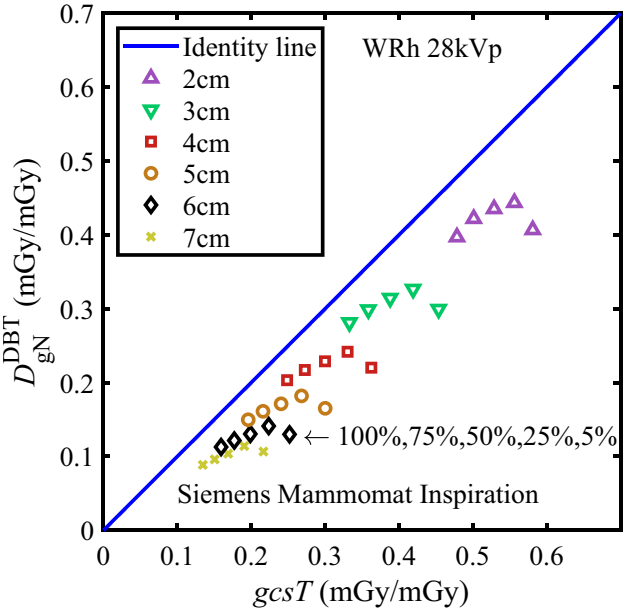


**Fig. 8** Comparison of the estimated $D_{gN}^{DBT}$ values for different CBTs and glandularities under the target/filter combination W/Rh 28 kVp of Siemens Mammomat Inspiration. The data of each group with the same CBT correspond to 100%, 75%, 50%, 25%, and 5% $P_g^M$ from left to right. The identity line indicates equal $D_{gN}^{DBT}$ values for the detailed and simple breast models. (Color figure online)

energy-deposited area was concentrated between breast depths of approximately 1 cm and 2 cm. The greatest discrepancy in $E_{gN}(z)$ between the detailed and simple breast models was found near the breast surface and was primarily associated with depth variations of $f_g(z)$. When considering detailed breast models with varying glandularities, the main energy deposition area depicted in Fig. 7c was marginally shallower than the depth associated with the highest concentration of $f_g(z)$ because of the exponential attenuation of the X-ray beam.

### 3.5 Literature comparison

As demonstrated in Sect. 3.3.1, a strong linear correlation exists between $D_{gN}^{DBT}$ and the HVL. By fitting the available data, we calculated the $D_{gN}^{DBT}$ values for other HVLs and compared them with the $D_{gN}^{DBT}$ values obtained by multiplying with gcsT, as provided by Dance. The relative differences Δ ranged from 18.6 to 51.0%, as summarized by CBTs and X-ray spectra. When the CBT and glandularity remained constant, Δ increased with HVL because a higher HVL beam is more penetrating. Figure 8 illustrates the $D_{gN}^{DBT}$ results for various CBT and glandularities. As the CBT increased and glandularity decreased, the corresponding points progressively deviated from the identity line. This indicates that Δ

decreases with increasing glandularity and increases with increasing CBT. The highest Δ value was observed for the breast model with 7 cm CBT and 5% glandularity.

## 4 Discussion

The high incidence of breast cancer in China necessitates accurate coefficients for glandular dose estimation in women undergoing breast screening. However, there are significant differences in the internal structures of Chinese and Western women [19, 20], and the dose estimation for Chinese women is based on dosimetry protocols developed using a simple breast model, which may result in an overestimation of $D_g$. Therefore, establishing dosimetry protocols for Chinese women would greatly improve the assessment of radiation risk in women during breast screening and contribute to increasing our understanding of racial differences in breast cancer risk.

In this study, we used Geant4 to calculate a series of conversion factors, $D_{gN}^{DBT}$, for four commercial DBT devices based on detailed breast models. Detailed breast models constructed based on representative breast parameters of the Chinese female population were combined with CRAF. Previous studies have agreed that beam conditions (target/filter combination and beam HVL) and breast characteristics (CBT and glandularity) are the main factors affecting $D_{gN}^{DBT}$, which are computed using simple breast models. This study examined the correlation between these factors using detailed breast models. $D_{gN}^{DBT}$ and HVL exhibited a good linear relationship although the detailed structure was heterogeneous. We found that $D_{gN}^{DBT}$ and CBT exhibited a bi-exponential attenuation relationship in detailed breast models, which is consistent with the findings of Sarno [39] based on simple breast models. It is worth noting that pressure affects CBT. Excessive pressure can lead to the thinning of the breast, which, in turn, reduces $D_{gN}^{DBT}$. A previous study demonstrated that $D_{gN}^{DBT}$ and glandularity have a perfect quadratic function relationship and $D_{gN}^{DBT}$ decreases with an increase in glandularity [39]. However, this study indicated that at lower glandularity, $D_{gN}^{DBT}$ increased with an increase in glandularity. This difference was mainly due to the assumptions made by the breast models during the generation process. We assumed that at lower glandularity, the glandular tissue mainly existed in the form of lactiferous ducts, which are random tree-like structures that grow from the lactiferous sinus at the nipple to the chest wall and are concentrated near the nipple within the breast [36]. When the patient's glandularity increased, adipose tissue in the fibroglandular region was gradually replaced by glandular tissue. Two changes occurred that affected $D_g$. First, the centroid of the glandular tissue gradually moved in the nipple–chest direction. This meant that the glandular area was closer to the X-ray source and received a higher glandular dose. Second, the exponential attenuation characteristic of $D_g^{dep}(z)$ caused the $D_g$ obtained using the breast model with 25% $P_g^M$ to be higher than that obtained using the breast model with 5% $P_g^M$. However, under the assumption of a homogeneous model, the transformation of 5–25% $P_g^M$ did not involve the gradual replacement of the glandular tissue, and the centroid of the glandular tissue always remained at the same position. The difference between the two assumptions resulted in different performances of $D_{gN}^{DBT}$ variation at low glandularities. It is worth mentioning that the parameter dependence of the breast characteristics and beam conditions on $D_{gN}^{DBT}$ based on a breast model with microstructure has not yet been documented. In addition, we compared the $D_{gN}^{DBT}$ of this study with those of the traditional protocol and found a difference of approximately 18.6–51.0%. Caballo et al. [12] compared the $D_{gN}$ of homogeneous models with that of real clinical patients, and the 25% and 75% quartiles of the difference were 26.3% and 56.4%, which are very close to our variation in $D_{gN}^{DBT}$. These comparative data indicate that the detailed breast model used can approximate a clinical patient's breast model.

We analyzed the distribution of the normalized deposited energy in the glandular region ($E_{gN}(z)$) along the depth direction for detailed and homogeneous breast models with 4-cm CBT and different glandularities. We found that the main energy deposition region of the detailed breast models was located in the upper area with a depth range of 1–2 cm. This area shifted to a shallower area in the simple breast models. The downward trend in the main energy deposition region will inevitably result in a decrease in $D_g$ and $D_{gN}^{DBT}$. As the CBT increases, the distance between the main energy deposition areas of the detailed and simple breast models also increases. This leads to a larger difference in $D_{gN}^{DBT}$ between the models with increasing CBT. Overall, this study indicated that the discrepancy between the $D_{gN}^{DBT}$ values obtained from the detailed and simple breast models increased with decreasing glandularity, increasing CBT, and increasing beam energy, as illustrated by Hernandez et al. [17] and Cordeiro de Souza et al. [13]. Meanwhile, $E_{gN}(z)$, a quantity that considers the amount and distribution or location of glandular tissue along the depth direction, contributed to the identification of high-risk areas within the breast during screening. Careful examination and monitoring are required in areas prone to cancer induction.

The method used to define glandularity in this study was not the same as that employed in other studies [12, 13, 39]. Dance's model includes an outer 5-mm adipose layer and a central glandular region. The researchers initially considered the outer 5-mm layer to be skin. However, as their understanding of breast anatomy gradually deepened, the thickness of the outer skin layer was found to be 1.45 mm and there was almost no glandular tissue in the subcutaneous adipose layer, which was approximately 3–4 mm thick. Although it is now widely accepted that the "5-mm skin" view is incorrect, the 5-mm adipose layer in Dance's model can be seen as a combination of skin (1.45 mm) and subcutaneous adipose (3–4 mm). Therefore, when defining $P_g^M$ in this study, we excluded the skin and subcutaneous adipose layers to make its physical meaning consistent with the glandularity in Dance's model [8, 16]. For comparison with other literature and for use in clinical dose calculations, this study also defined the concept of breast volume density to measure the proportion of glands in the entire breast.

Admittedly, it is necessary to recognize that this study has several limitations. The detailed breast model was mainly developed based on the representative breast parameters (including breast shape, CBT, glandularity, skin thickness, and subcutaneous adipose thickness) of Chinese women. However, we lacked high-resolution clinical images of Chinese women for more accurate parameter information. Research has indicated that different types of glandular distributions have an important impact on dose conversion coefficients, especially the location of the concentrated area of the glandular tissue [13]. In their study on clinical DBCT images, Fedon [18] found that glandular distribution is not symmetrical along the depth direction, with the center being biased downward in the depth direction. Therefore, obtaining accurate glandular distributions for Chinese women of different age groups is an important direction for future research. In this study, $D_{gN}^{DBT}$ exhibited an upward trend at lower glandularity levels. This indicates that the growth characteristics of the lactiferous ducts also significantly affect the calculation results for $D_{gN}^{DBT}$. However, the effect of this factor requires further investigation. It is worth mentioning that these detailed breast models can also provide images with texture. Based on the anthropopathic characteristics of the detailed breast model, we can investigate the association between image quality and radiation risk in the future and use this to obtain optimal exposure parameters for individual patients.

## 5 Conclusion

This study aimed to provide $D_{gN}^{DBT}$ values for four commercial DBT systems that are widely used in China. Based on a detailed breast model combined with CRAF, the dependence of $D_{gN}^{DBT}$ on various parameters, including the beam condition (target/filter combination, beam HVL) and breast characteristics (CBT and glandularity), which have not yet been documented, was investigated. The calculated results deviated by up to 18.6% and 51.0% from data obtained using the traditional dosimetry protocol. We also proposed a physical quantity, $E_{gN}(z)$, to analyze the difference in $D_{gN}^{DBT}$ in breast models with different glandular distributions and to roughly determine the range of breast depth with high cancer risk. This study contributes to the improvement of breast dosimetry protocols for DBT in China. The $D_{gN}^{DBT}$ tabulations obtained in this study provide a powerful tool for the rapid and straightforward assessment of $D_g$ in Chinese females undergoing DBT scanning. However, it has certain limitations owing to the lack of clinical data. Another aspect to explore in the future involves obtaining the breast characteristics (including glandular distribution, glandularity, and breast size) of Chinese females in different age groups.

## Appendix A

See Tables 4, 5, 6, 7 and 8.

**Table 4** Target/filter combination W/Rh of Siemens Mammomat Inspiration

| HVL (mmAl) | CBT (cm) | $P_g^M$ | | | | |
|---|---|---|---|---|---|---|
| | | 5% | 25% | 50% | 75% | 100% |
| 0.508 | 2 | 0.415 | 0.449 | 0.442 | 0.428 | 0.402 |
| 0.508 | 3 | 0.306 | 0.334 | 0.320 | 0.305 | 0.287 |
| 0.508 | 4 | 0.228 | 0.251 | 0.237 | 0.225 | 0.210 |
| 0.508 | 5 | 0.173 | 0.191 | 0.179 | 0.168 | 0.156 |
| 0.508 | 6 | 0.135 | 0.148 | 0.137 | 0.128 | 0.119 |
| 0.508 | 7 | 0.114 | 0.121 | 0.110 | 0.103 | 0.095 |
| 0.544 | 2 | 0.434 | 0.473 | 0.466 | 0.452 | 0.424 |
| 0.544 | 3 | 0.330 | 0.358 | 0.344 | 0.329 | 0.309 |
| 0.544 | 4 | 0.249 | 0.272 | 0.258 | 0.245 | 0.229 |
| 0.544 | 5 | 0.191 | 0.208 | 0.196 | 0.184 | 0.171 |
| 0.544 | 6 | 0.153 | 0.165 | 0.153 | 0.143 | 0.132 |
| 0.544 | 7 | 0.127 | 0.136 | 0.124 | 0.115 | 0.107 |
| 0.568 | 2 | 0.440 | 0.480 | 0.473 | 0.458 | 0.430 |
| 0.568 | 3 | 0.336 | 0.366 | 0.352 | 0.336 | 0.315 |
| 0.568 | 4 | 0.257 | 0.279 | 0.265 | 0.252 | 0.235 |
| 0.568 | 5 | 0.198 | 0.217 | 0.204 | 0.192 | 0.179 |
| 0.568 | 6 | 0.160 | 0.172 | 0.160 | 0.149 | 0.138 |
| 0.568 | 7 | 0.135 | 0.143 | 0.130 | 0.121 | 0.112 |
| 0.584 | 2 | 0.448 | 0.488 | 0.481 | 0.467 | 0.438 |
| 0.584 | 3 | 0.345 | 0.377 | 0.363 | 0.346 | 0.325 |
| 0.584 | 4 | 0.263 | 0.288 | 0.273 | 0.259 | 0.242 |
| 0.584 | 5 | 0.204 | 0.223 | 0.210 | 0.198 | 0.185 |
| 0.584 | 6 | 0.164 | 0.178 | 0.165 | 0.155 | 0.143 |
| 0.584 | 7 | 0.138 | 0.147 | 0.135 | 0.126 | 0.117 |
| 0.609 | 2 | 0.460 | 0.501 | 0.493 | 0.478 | 0.448 |
| 0.609 | 3 | 0.355 | 0.389 | 0.376 | 0.357 | 0.336 |
| 0.609 | 4 | 0.276 | 0.298 | 0.285 | 0.270 | 0.253 |
| 0.609 | 5 | 0.216 | 0.234 | 0.221 | 0.209 | 0.195 |
| 0.609 | 6 | 0.175 | 0.188 | 0.176 | 0.165 | 0.153 |
| 0.609 | 7 | 0.148 | 0.158 | 0.145 | 0.135 | 0.125 |
| 0.690 | 2 | 0.495 | 0.542 | 0.534 | 0.518 | 0.485 |
| 0.690 | 3 | 0.395 | 0.433 | 0.420 | 0.399 | 0.374 |
| 0.690 | 4 | 0.314 | 0.337 | 0.322 | 0.306 | 0.286 |
| 0.690 | 5 | 0.248 | 0.268 | 0.255 | 0.241 | 0.225 |
| 0.690 | 6 | 0.205 | 0.219 | 0.206 | 0.193 | 0.179 |
| 0.690 | 7 | 0.175 | 0.186 | 0.172 | 0.160 | 0.148 |

**Table 5** Target/filter combination W/Al of Hologic Selenia dimensions

| HVL(mmAl) | CBT (cm) | $P_g^M$ | | | | |
|---|---|---|---|---|---|---|
| | | 5% | 25% | 50% | 75% | 100% |
| 0.458 | 2 | 0.403 | 0.441 | 0.432 | 0.419 | 0.394 |
| 0.458 | 3 | 0.297 | 0.324 | 0.312 | 0.297 | 0.280 |
| 0.458 | 4 | 0.218 | 0.240 | 0.227 | 0.216 | 0.202 |
| 0.458 | 5 | 0.164 | 0.181 | 0.170 | 0.160 | 0.149 |
| 0.458 | 6 | 0.129 | 0.140 | 0.130 | 0.121 | 0.112 |
| 0.458 | 7 | 0.106 | 0.114 | 0.104 | 0.096 | 0.089 |
| 0.529 | 2 | 0.449 | 0.487 | 0.481 | 0.466 | 0.438 |
| 0.529 | 3 | 0.342 | 0.371 | 0.360 | 0.342 | 0.321 |
| 0.529 | 4 | 0.260 | 0.285 | 0.271 | 0.257 | 0.241 |
| 0.529 | 5 | 0.201 | 0.220 | 0.209 | 0.197 | 0.183 |
| 0.529 | 6 | 0.162 | 0.177 | 0.165 | 0.154 | 0.143 |
| 0.529 | 7 | 0.135 | 0.144 | 0.133 | 0.124 | 0.114 |
| 0.576 | 2 | 0.474 | 0.514 | 0.508 | 0.493 | 0.463 |
| 0.576 | 3 | 0.367 | 0.399 | 0.387 | 0.369 | 0.346 |
| 0.576 | 4 | 0.283 | 0.310 | 0.296 | 0.281 | 0.263 |
| 0.576 | 5 | 0.223 | 0.242 | 0.231 | 0.218 | 0.203 |
| 0.576 | 6 | 0.180 | 0.197 | 0.185 | 0.173 | 0.161 |
| 0.576 | 7 | 0.152 | 0.163 | 0.151 | 0.141 | 0.130 |
| 0.624 | 2 | 0.493 | 0.536 | 0.530 | 0.515 | 0.483 |
| 0.624 | 3 | 0.391 | 0.422 | 0.410 | 0.391 | 0.367 |
| 0.624 | 4 | 0.305 | 0.332 | 0.319 | 0.303 | 0.283 |
| 0.624 | 5 | 0.243 | 0.264 | 0.252 | 0.238 | 0.221 |
| 0.624 | 6 | 0.198 | 0.216 | 0.203 | 0.191 | 0.177 |
| 0.624 | 7 | 0.167 | 0.179 | 0.167 | 0.155 | 0.144 |
| 0.696 | 2 | 0.518 | 0.561 | 0.558 | 0.542 | 0.507 |
| 0.696 | 3 | 0.413 | 0.450 | 0.439 | 0.419 | 0.392 |
| 0.696 | 4 | 0.329 | 0.359 | 0.345 | 0.328 | 0.307 |
| 0.696 | 5 | 0.265 | 0.288 | 0.276 | 0.261 | 0.243 |
| 0.696 | 6 | 0.218 | 0.239 | 0.226 | 0.212 | 0.197 |
| 0.696 | 7 | 0.188 | 0.201 | 0.188 | 0.176 | 0.163 |
| 0.841 | 2 | 0.594 | 0.641 | 0.641 | 0.623 | 0.582 |
| 0.841 | 3 | 0.492 | 0.533 | 0.522 | 0.499 | 0.466 |
| 0.841 | 4 | 0.402 | 0.438 | 0.423 | 0.402 | 0.376 |
| 0.841 | 5 | 0.333 | 0.359 | 0.346 | 0.327 | 0.305 |
| 0.841 | 6 | 0.277 | 0.303 | 0.288 | 0.272 | 0.252 |
| 0.841 | 7 | 0.241 | 0.258 | 0.242 | 0.227 | 0.210 |

**Table 6** Target/filter combination Mo/Mo of GE SenoClaire and GE Senographe Pristina

| HVL (mmAl) | CBT (cm) | $P_g^M$ | | | | |
|---|---|---|---|---|---|---|
| | | 5% | 25% | 50% | 75% | 100% |
| 0.351 | 2 | 0.326 | 0.357 | 0.346 | 0.336 | 0.317 |
| 0.351 | 3 | 0.223 | 0.247 | 0.235 | 0.223 | 0.210 |
| 0.351 | 4 | 0.156 | 0.175 | 0.163 | 0.154 | 0.145 |
| 0.351 | 5 | 0.112 | 0.125 | 0.117 | 0.109 | 0.102 |
| 0.351 | 6 | 0.085 | 0.094 | 0.086 | 0.079 | 0.074 |
| 0.351 | 7 | 0.069 | 0.074 | 0.066 | 0.060 | 0.056 |
| 0.384 | 2 | 0.350 | 0.383 | 0.373 | 0.361 | 0.341 |
| 0.384 | 3 | 0.246 | 0.271 | 0.259 | 0.247 | 0.232 |
| 0.384 | 4 | 0.174 | 0.194 | 0.182 | 0.172 | 0.162 |
| 0.384 | 5 | 0.126 | 0.141 | 0.132 | 0.123 | 0.115 |
| 0.384 | 6 | 0.098 | 0.108 | 0.099 | 0.091 | 0.085 |
| 0.384 | 7 | 0.079 | 0.085 | 0.076 | 0.070 | 0.065 |
| 0.403 | 2 | 0.363 | 0.398 | 0.388 | 0.376 | 0.355 |
| 0.403 | 3 | 0.259 | 0.285 | 0.272 | 0.259 | 0.244 |
| 0.403 | 4 | 0.185 | 0.206 | 0.193 | 0.183 | 0.172 |
| 0.403 | 5 | 0.136 | 0.152 | 0.141 | 0.133 | 0.123 |
| 0.403 | 6 | 0.105 | 0.115 | 0.106 | 0.098 | 0.091 |
| 0.403 | 7 | 0.086 | 0.092 | 0.083 | 0.076 | 0.070 |
| 0.419 | 2 | 0.374 | 0.410 | 0.399 | 0.388 | 0.365 |
| 0.419 | 3 | 0.268 | 0.296 | 0.283 | 0.269 | 0.253 |
| 0.419 | 4 | 0.195 | 0.215 | 0.202 | 0.192 | 0.180 |
| 0.419 | 5 | 0.143 | 0.159 | 0.148 | 0.139 | 0.130 |
| 0.419 | 6 | 0.111 | 0.122 | 0.112 | 0.104 | 0.096 |
| 0.419 | 7 | 0.091 | 0.097 | 0.088 | 0.081 | 0.075 |
| 0.439 | 2 | 0.388 | 0.423 | 0.414 | 0.401 | 0.378 |
| 0.439 | 3 | 0.281 | 0.308 | 0.294 | 0.281 | 0.264 |
| 0.439 | 4 | 0.205 | 0.226 | 0.213 | 0.202 | 0.189 |
| 0.439 | 5 | 0.153 | 0.169 | 0.158 | 0.148 | 0.138 |
| 0.439 | 6 | 0.119 | 0.130 | 0.120 | 0.112 | 0.104 |
| 0.439 | 7 | 0.098 | 0.104 | 0.095 | 0.088 | 0.081 |
| 0.474 | 2 | 0.413 | 0.451 | 0.442 | 0.428 | 0.403 |
| 0.474 | 3 | 0.305 | 0.334 | 0.320 | 0.305 | 0.286 |
| 0.474 | 4 | 0.225 | 0.247 | 0.233 | 0.221 | 0.207 |
| 0.474 | 5 | 0.169 | 0.187 | 0.174 | 0.164 | 0.153 |
| 0.474 | 6 | 0.132 | 0.144 | 0.133 | 0.125 | 0.116 |
| 0.474 | 7 | 0.109 | 0.116 | 0.106 | 0.098 | 0.091 |

**Table 7** Target/filter combination Rh/Rh of GE SenoClaire

| HVL (mmAl) | CBT (cm) | $P_g^M$ | | | | |
|---|---|---|---|---|---|---|
| | | 5% | 25% | 50% | 75% | 100% |
| 0.393 | 2 | 0.347 | 0.380 | 0.371 | 0.360 | 0.340 |
| 0.393 | 3 | 0.249 | 0.273 | 0.262 | 0.249 | 0.235 |
| 0.393 | 4 | 0.179 | 0.198 | 0.187 | 0.177 | 0.166 |
| 0.393 | 5 | 0.133 | 0.148 | 0.138 | 0.129 | 0.121 |
| 0.393 | 6 | 0.104 | 0.114 | 0.104 | 0.097 | 0.090 |
| 0.393 | 7 | 0.084 | 0.090 | 0.082 | 0.076 | 0.070 |
| 0.446 | 2 | 0.378 | 0.411 | 0.402 | 0.390 | 0.368 |
| 0.446 | 3 | 0.277 | 0.304 | 0.292 | 0.278 | 0.261 |
| 0.446 | 4 | 0.206 | 0.226 | 0.213 | 0.202 | 0.189 |
| 0.446 | 5 | 0.156 | 0.171 | 0.161 | 0.151 | 0.141 |
| 0.446 | 6 | 0.123 | 0.133 | 0.124 | 0.115 | 0.107 |
| 0.446 | 7 | 0.102 | 0.108 | 0.099 | 0.092 | 0.085 |
| 0.481 | 2 | 0.393 | 0.427 | 0.420 | 0.407 | 0.383 |
| 0.481 | 3 | 0.293 | 0.320 | 0.308 | 0.293 | 0.276 |
| 0.481 | 4 | 0.220 | 0.241 | 0.229 | 0.217 | 0.204 |
| 0.481 | 5 | 0.164 | 0.185 | 0.175 | 0.164 | 0.153 |
| 0.481 | 6 | 0.134 | 0.145 | 0.135 | 0.126 | 0.116 |
| 0.481 | 7 | 0.111 | 0.119 | 0.109 | 0.101 | 0.093 |
| 0.508 | 2 | 0.407 | 0.442 | 0.436 | 0.423 | 0.397 |
| 0.508 | 3 | 0.307 | 0.334 | 0.323 | 0.307 | 0.288 |
| 0.508 | 4 | 0.231 | 0.254 | 0.242 | 0.229 | 0.214 |
| 0.508 | 5 | 0.178 | 0.195 | 0.184 | 0.173 | 0.161 |
| 0.508 | 6 | 0.143 | 0.155 | 0.144 | 0.135 | 0.125 |
| 0.508 | 7 | 0.120 | 0.128 | 0.117 | 0.108 | 0.100 |
| 0.545 | 2 | 0.419 | 0.455 | 0.449 | 0.436 | 0.409 |
| 0.545 | 3 | 0.320 | 0.348 | 0.337 | 0.321 | 0.301 |
| 0.545 | 4 | 0.244 | 0.268 | 0.254 | 0.241 | 0.226 |
| 0.545 | 5 | 0.193 | 0.209 | 0.197 | 0.186 | 0.173 |
| 0.545 | 6 | 0.154 | 0.166 | 0.155 | 0.145 | 0.135 |
| 0.545 | 7 | 0.128 | 0.137 | 0.126 | 0.117 | 0.108 |
| 0.625 | 2 | 0.460 | 0.498 | 0.494 | 0.479 | 0.449 |
| 0.625 | 3 | 0.360 | 0.390 | 0.378 | 0.361 | 0.338 |
| 0.625 | 4 | 0.281 | 0.306 | 0.292 | 0.278 | 0.260 |
| 0.625 | 5 | 0.223 | 0.242 | 0.229 | 0.217 | 0.202 |
| 0.625 | 6 | 0.181 | 0.195 | 0.183 | 0.171 | 0.159 |
| 0.625 | 7 | 0.153 | 0.163 | 0.150 | 0.140 | 0.129 |

**Table 8** Target/filter combination Rh/Ag of GE Senographe Pristina

| HVL (mmAl) | CBT (cm) | $P_g^M$ | | | | |
|---|---|---|---|---|---|---|
| | | 5% | 25% | 50% | 75% | 100% |
| 0.511 | 2 | 0.397 | 0.433 | 0.425 | 0.412 | 0.388 |
| 0.511 | 3 | 0.296 | 0.324 | 0.311 | 0.296 | 0.278 |
| 0.511 | 4 | 0.220 | 0.243 | 0.229 | 0.218 | 0.204 |
| 0.511 | 5 | 0.171 | 0.186 | 0.174 | 0.164 | 0.152 |
| 0.511 | 6 | 0.137 | 0.146 | 0.136 | 0.127 | 0.118 |
| 0.511 | 7 | 0.115 | 0.121 | 0.110 | 0.102 | 0.094 |
| 0.590 | 2 | 0.432 | 0.470 | 0.462 | 0.448 | 0.421 |
| 0.590 | 3 | 0.332 | 0.360 | 0.348 | 0.331 | 0.311 |
| 0.590 | 4 | 0.253 | 0.277 | 0.263 | 0.250 | 0.233 |
| 0.590 | 5 | 0.199 | 0.217 | 0.205 | 0.192 | 0.179 |
| 0.590 | 6 | 0.163 | 0.174 | 0.161 | 0.151 | 0.140 |
| 0.590 | 7 | 0.138 | 0.145 | 0.133 | 0.123 | 0.114 |
| 0.620 | 2 | 0.446 | 0.485 | 0.479 | 0.465 | 0.436 |
| 0.620 | 3 | 0.346 | 0.374 | 0.361 | 0.344 | 0.323 |
| 0.620 | 4 | 0.267 | 0.290 | 0.276 | 0.262 | 0.245 |
| 0.620 | 5 | 0.212 | 0.228 | 0.215 | 0.203 | 0.189 |
| 0.620 | 6 | 0.172 | 0.185 | 0.172 | 0.161 | 0.149 |
| 0.620 | 7 | 0.146 | 0.153 | 0.141 | 0.131 | 0.121 |
| 0.646 | 2 | 0.454 | 0.493 | 0.487 | 0.473 | 0.443 |
| 0.646 | 3 | 0.354 | 0.383 | 0.371 | 0.354 | 0.332 |
| 0.646 | 4 | 0.275 | 0.299 | 0.285 | 0.271 | 0.253 |
| 0.646 | 5 | 0.218 | 0.235 | 0.223 | 0.210 | 0.195 |
| 0.646 | 6 | 0.177 | 0.190 | 0.177 | 0.166 | 0.154 |
| 0.646 | 7 | 0.153 | 0.160 | 0.147 | 0.137 | 0.127 |
| 0.676 | 2 | 0.462 | 0.501 | 0.494 | 0.480 | 0.450 |
| 0.676 | 3 | 0.365 | 0.395 | 0.383 | 0.365 | 0.342 |
| 0.676 | 4 | 0.285 | 0.310 | 0.295 | 0.280 | 0.262 |
| 0.676 | 5 | 0.226 | 0.245 | 0.232 | 0.219 | 0.204 |
| 0.676 | 6 | 0.186 | 0.199 | 0.186 | 0.174 | 0.162 |
| 0.676 | 7 | 0.160 | 0.168 | 0.154 | 0.144 | 0.133 |
| 0.742 | 2 | 0.492 | 0.532 | 0.527 | 0.512 | 0.479 |
| 0.742 | 3 | 0.395 | 0.424 | 0.413 | 0.394 | 0.369 |
| 0.742 | 4 | 0.313 | 0.338 | 0.323 | 0.307 | 0.287 |
| 0.742 | 5 | 0.250 | 0.271 | 0.257 | 0.242 | 0.225 |
| 0.742 | 6 | 0.207 | 0.221 | 0.207 | 0.195 | 0.180 |
| 0.742 | 7 | 0.178 | 0.188 | 0.173 | 0.162 | 0.150 |

**Acknowledgements** The calculations in this study were supported by the High-Performance Computing Center at Tsinghua University.

**Author contribution** All authors contributed to the study conception and design. Material preparation, data collection and analysis were performed by Jia-Hao Wang, Rui Qiu, and An-Kang Hu. The first draft of the manuscript was written by Jia-Hao Wang and all authors commented on previous versions of the manuscript. All authors read and approved the final manuscript.

**Data availability** The data that support the findings of this study are openly available in Science Data Bank at https://cstr.cn/31253.11.sciencedb.j00186.00385 and https://doi.org/10.57760/sciencedb.j00186.00385.

## Declarations

**Conflict of interest** The authors declare that they have no competing interests.

## References


1. W. Chen, R. Zheng, P. Baade et al., Cancer statistics: updated cancer burden in China preface. Chin. J. Cancer Res. **27**, 1 (2015). https://doi.org/10.3978/j.issn.1000-9604.2015.02.07
2. C.P. Wild, E. Weiderpass, B.W. Stewart, *World Cancer Report: Cancer Research for Cancer Prevention* (International Agency for Research on Cancer, Lyon, 2020)
3. S. Lei, R. Zheng, S. Zhang et al., Breast cancer incidence and mortality in women in China: temporal trends and projections to 2030. Cancer Biol. Med. **18**, 900 (2021). https://doi.org/10.20892/j.issn.2095-3941.2020.0523
4. Y. Yang, L. Li, Z.Q. Chen, A review of geometric calibration for different 3D X-ray imaging systems. Nucl. Sci. Tech. **27**, 76 (2016). https://doi.org/10.1007/s41365-016-0073-y
5. S.M. Guo, J.J. Wu, D.J. Hou, The development, performances and applications of the monochromatic X-rays facilities in (0.218–301) keV at NIM China. Nucl. Sci. Tech. **32**, 65 (2021). https://doi.org/10.1007/s41365-021-00890-2
6. ICRP, The 2007 recommendations of the international commission on radiological protection (2007)
7. D.R. Dance, I. Sechopoulos, Dosimetry in x-ray-based breast imaging. Phys. Med. Biol. **61**, R271 (2016). https://doi.org/10.1088/0031-9155/61/19/r271
8. D.R. Dance, K.C. Young, R.E. van Engen, Further factors for the estimation of mean glandular dose using the United Kingdom, European and IAEA breast dosimetry protocols. Phys. Med. Biol. **54**, 4361 (2009). https://doi.org/10.1088/0031-9155/54/14/002
9. D.R. Dance, K.C. Young, R.E. van Engen, Estimation of mean glandular dose for breast tomosynthesis: factors for use with the UK, European and IAEA breast dosimetry protocols. Phys. Med. Biol. **56**, 453 (2011). https://doi.org/10.1088/0031-9155/56/2/011
10. I. Sechopoulos, K. Bliznakova, X.L. Qin et al., Characterization of the homogeneous tissue mixture approximation in breast imaging dosimetry. Med. Phys. **39**, 5050 (2012). https://doi.org/10.1118/1.4737025
11. A. Sarno, G. Mettivier, F. Di Lillo et al., Homogeneous vs. patient specific breast models for Monte Carlo evaluation of mean glandular dose in mammography. Phys. Med. **51**, 56 (2018). https://doi.org/10.1016/j.ejmp.2018.04.392
12. M. Caballo, C. Rabin, C. Fedon et al., Patient-derived heterogeneous breast phantoms for advanced dosimetry in mammography and tomosynthesis. Med. Phys. **49**, 5423 (2022). https://doi.org/10.1002/mp.15785
13. G. Ferrauche, G. Tramontin, R.T. Massera et al., Impact of fibroglandular tissue distribution and breast shape in voxelized breast models for dosimetry in mammography. Phys. Med. Biol. **68**, 074003 (2023). https://doi.org/10.1088/1361-6560/acbefd
14. J.M. Boone, A.M. Hernandez, A. Seibert, Two-dimensional breast dosimetry improved using three-dimensional breast image data. Radiol. Phys. Technol. **10**, 129 (2017). https://doi.org/10.1007/s12194-017-0404-7
15. R.T. Massera, A. Tomal, Skin models and their impact on mean glandular dose in mammography. Phys. Med. **51**, 38 (2018). https://doi.org/10.1016/j.ejmp.2018.04.009
16. D.R. Dance, R.A. Hunt, P.R. Bakic et al., Breast dosimetry using high-resolution voxel phantoms. Radiat. Prot. Dosim. **114**, 359 (2005). https://doi.org/10.1093/rpd/nch510
17. A.M. Hernandez, J.A. Seibert, J.M. Boone, Breast dose in mammography is about 30% lower when realistic heterogeneous glandular distributions are considered. Med. Phys. **42**, 6337 (2015). https://doi.org/10.1118/1.4931966
18. C. Fedon, M. Caballo, E. Garcia et al., Fibroglandular tissue distribution in the breast during mammography and tomosynthesis based on breast CT data: a patient-based characterization of the breast parenchyma. Med. Phys. **48**, 1436 (2021). https://doi.org/10.1002/mp.14716
19. M.G. del Carmen, E.F. Halpern, D.B. Kopans et al., Mammographic breast density and race. Am. J. Roentgenol. **188**, 1147 (2007). https://doi.org/10.2214/ajr.06.0619
20. J.H. Wang, R. Qiu, A.K. Hu et al., Preliminary imaging study on the distribution of female volumetric breast density. Chin. J. Radiol. Med. Prot. **42**, 806 (2022)
21. R.Y. Ma, R. Qiu, Z. Wu et al., Development of Chinese mesh-type pediatric reference phantom series and application in dose assessment of Chinese undergoing computed tomography scanning. Phys. Med. Biol. **66**, 195002 (2021). https://doi.org/10.1088/1361-6560/ac1ef1
22. X.Y. Luo, R. Qiu, Z. Wu et al., A body-size-dependent series of Chinese adult standing phantoms for radiation dosimetry. J. Radiol. Prot. **43**, 011501 (2023). https://doi.org/10.1088/1361-6498/acad0d
23. L. Liu, Z. Zeng, J. Li et al., Organ dose conversion coefficients on an ICRP-based Chinese adult male voxel model from idealized external photons exposures. Phys. Med. Biol. **54**, 6645 (2009). https://doi.org/10.1088/0031-9155/54/21/014
24. W. Lu, R. Qiu, Z. Wu et al., Calculation of conversion coefficients using Chinese adult reference phantoms for air submersion and ground contamination. Phys. Med. Biol. **62**, 2276 (2017). https://doi.org/10.1088/1361-6560/aa5c31
25. S.Y. Huang, J.M. Boone, K. Yang et al., The characterization of breast anatomical metrics using dedicated breast CT. Med. Phys. **38**, 2180 (2011). https://doi.org/10.1118/1.3567147
26. R. Tucciariello, P. Barca, D. Sarto et al., Voxelized breast phantoms for dosimetry in mammography. *Paper Presented at 14th International Joint Conference on Biomedical Engineering Systems and Technologies (BIOSTEC)/12th International Conference on Bioinformatics Models, Methods and Algorithms (BIOINFORMATICS)* (Electr Network, Feb 11–13)
27. National Health Commission of the People's Republic of China, Methods for estimation of examinee's organ doses in X-ray diagnosis (2021)
28. W.J. Wang, R. Qiu, L. Ren et al., Monte Carlo calculation of conversion coefficients for dose estimation in mammography based on a 3D detailed breast model. Med. Phys. **44**, 2503 (2017). https://doi.org/10.1002/mp.12210
29. R. Qiu, C.X. Jiang, L. Ren et al., Establishment of the detailed breast model of Chinese adult female and application in external radiation protection. Radiat. Prot. Dosim. **174**, 113 (2017). https://doi.org/10.1093/rpd/ncw092
30. W.J. Wang, R. Qiu, L. Ren et al., Detailed breast model and its application to glandular dose estimation in mammography. At. Energy Sci. Technol. (in Chinese) **50**, 2085 (2016)
31. L. Ren, R. Qiu, J. Li, Establishment of the detailed breast model of Chinese adult female and its application in external radiation protection. Radiat. Prot. **36**, 65 (2016)
32. L. Ren, R. Qiu, J. Li et al., A detailed breast model and its application for Chinese female breast dose estimation in mammography. *Paper Presented at Joint 8th International Conference on Supercomputing in Nuclear Applications (SNA)/4th Monte Carlo Meeting (MC)* (Paris, France, 2014)
33. EUREF, Protocol for the quality control of the physical and technical aspects of digital breast tomosynthesis systems. Version 1.03 (2018). [Available from: https://euref.org/european-guidelines/physico-technical-protocol#breasttomo
34. W.J. Wang, R. Qiu, L. Ren et al., dose distribution in a breast undergoing mammography based on a 3D detailed breast model for Chinese women. Radiat. Prot. Dosim. **181**, 221 (2018). https://doi.org/10.1093/rpd/ncy017
35. D.R. Dance, C.L. Skinner, K.C. Young et al., Additional factors for the estimation of mean glandular breast dose using the UK

mammography dosimetry protocol. Phys. Med. Biol. **45**, 3225 (2000). https://doi.org/10.1088/0031-9155/45/11/308
36. D.T. Ramsay, J.C. Kent, R.A. Hartmann et al., Anatomy of the lactating human breast redefined with ultrasound imaging. J. Anat. **206**, 525 (2005). https://doi.org/10.1111/j.1469-7580.2005.00417.x
37. P.R. Bakic, M. Albert, D. Brzakovic et al., Mammogram synthesis using a 3D simulation. 1. Breast tissue model and image acquisition simulation. Med. Phys. **29**, 2131 (2002). https://doi.org/10.1118/1.1501143
38. D.M. Mahr, R. Bhargava, M.F. Insana, Three-dimensional in silico breast phantoms for multimodal image simulations. IEEE Trans. Med. Imaging **31**, 689 (2012). https://doi.org/10.1109/tmi.2011.2175401
39. A. Sarno, R.M. Tucciariello, G. Mettivier et al., Normalized glandular dose coefficients for digital breast tomosynthesis systems with a homogeneous breast model. Phys. Med. Biol. **66**, 065024 (2021). https://doi.org/10.1088/1361-6560/abe2e9
40. D.R. Dance, K.C. Young, Estimation of mean glandular dose for contrast enhanced digital mammography: factors for use with the UK, European and IAEA breast dosimetry protocols. Phys. Med. Biol. **59**, 2127 (2014). https://doi.org/10.1088/0031-9155/59/9/2127
41. S. Agostinelli, J. Allison, K. Amako et al., Geant4—a simulation toolkit. Nucl. Instrum. Meth. Phys. Res. Sect. A **506**, 250 (2003). https://doi.org/10.1016/S0168-9002(03)01368-8
42. Python, A dynamic, open source programming language (Python software foundation) (2019). Available from: https://python.org/
43. ICRU, Photon, electron, proton and neutron interaction data for body tissues (1992). Report No.: ICRU Report 46
44. J.M. Boone, T.R. Fewell, R.J. Jennings, Molybdenum, rhodium, and tungsten anode spectral models using interpolating polynomials with application to mammography. Med. Phys. **24**, 1863 (1997). https://doi.org/10.1118/1.598100
45. A.M. Hernandez, J.A. Seibert, A. Nosratieh et al., Generation and analysis of clinically relevant breast imaging x-ray spectra. Med. Phys. **44**, 2148 (2017). https://doi.org/10.1002/mp.12222